THE ASTROPHYSICAL JOURNAL, 454:217–232, 1995 November 20

COLLAPSE CANDIDATES AMONG THE BOK GLOBULES

YANGSHENG WANG,[1,2] NEAL J. EVANS II,[1] SHUDONG ZHOU,[1,3,4] AND DAN P. CLEMENS[5]
Received 1995 February 27; accepted 1995 June 5

ABSTRACT

A survey in the $C^{18}O$ $J = 2 \rightarrow 1$ line toward Bok globules detected emission in 27 of them. Maps of the $C^{18}O$ line located maxima of column density within 34″ of *IRAS* sources in 12 globules. Emission in the H_2CO $J_{K_{-1}K_1} = 3_{12} \rightarrow 2_{11}$ line was detected toward nine of these 12 globules, indicating high volume density. Three of these sources have kinematic signatures consistent with collapse, as confirmed by detailed source modeling. Uncertainties in the distances make a definitive judgment about collapse difficult at this time, but we consider CB 244, CB 54, and CB 3 to be candidates for collapse. Among the three, CB 244 is the best example of low-mass star formation; CB 54 has the least convincing evidence for collapse but is worthy of further investigation; and CB 3 most likely represents intermediate-mass star formation.

Subject headings: ISM: globules — ISM: kinematics and dynamics — ISM: molecules

1. INTRODUCTION

The view that stars form via gravitational collapse of portions of molecular clouds is widely accepted, but actual kinematic evidence of collapse is scarce. Theoretical models of gravitational collapse, such as the inside-out collapse model (Shu 1977; Shu, Adams, & Lizano 1987), make specific, testable predictions about density and velocity fields in regions containing collapsing protostars. It is important to test the predictions of the collapse models, preferably in simple clouds, where observations are easy to interpret. The study of simple clouds is a good way to accumulate evidence for gravitational collapse and is a prerequisite to understanding star formation in complex, massive clouds, where the collapse signatures may be obscured by other processes.

Bok globules are excellent laboratories for such a study. They are relatively isolated molecular clouds, revealing themselves as roundish patches of enhanced visual extinction against the background stellar distribution. Optical studies using star-count techniques have indicated that some Bok globules are centrally condensed (Schmidt 1975; Bok & McCarthy 1974; Tomita, Saito, & Ohtani 1979), lending support to the suggestion that globules are in the process of gravitational collapse (see Bok & Reilly 1947; Bok 1948). Early molecular-line studies of Bok globules (Dickman 1976; Rickard et al. 1977; Martin & Barrett 1978) also have suggested that some globules are unstable against gravitational collapse (see Villere & Black 1980; Leung, Kutner, & Mead 1982). Direct evidence of ongoing star formation was first found in the Bok globule B335, where Keene et al. (1983) detected far-infrared continuum emission. More general evidence for star formation in globules came from studies utilizing the *IRAS* database (Clemens, Yun, & Heyer 1991; Yun & Clemens 1990). In particular, Yun & Clemens (1990) studied a sample of 248 Bok globules from a catalog by Clemens & Barvainis (1988; hereafter CB) and found that about 23% of the globules had associated *IRAS* point sources. These *IRAS* sources predominantly have colors and spectral energy distributions typical of embedded stellar or protostellar objects. Furthermore, about 30% of the globules with *IRAS* point sources were found to have CO outflows (Yun & Clemens 1992), confirming the star-forming activity in these simple clouds.

Recently, Zhou et al. (1990, 1993, 1994a) have argued that B335 exhibits the density and velocity structures predicted for gravitational collapse. In particular, the profiles of several molecular lines tracing dense gas were found to be consistent with theoretical models of inside-out collapse (Shu 1977). Interferometric observations of other lines and continuum emission are also consistent with the collapse interpretation (Chandler & Sargent 1993), as is a more self-consistent modeling of the line profiles (Choi et al. 1995).

It is important to learn if other Bok globules exhibit collapse signatures. We selected a sample of globules with associated *IRAS* sources and outflows found by Yun & Clemens (1990, 1992). We first located column density peaks in these globules, using $C^{18}O$. Observations of H_2CO toward peaks of column density were then used to identify regions of high density and line profiles characteristic of collapse.

1.1. *Collapse Signatures*

In an isothermal, quiescent, dense core, as depicted by Lizano & Shu (1989), the turbulent velocity decreases as the density increases. Hence, for a quiescent core with a centrally peaked density distribution, the line broadening is smaller in the center than in the outer region, consistent with the observed relation between line width and size of cores (Fuller & Myers 1992). As we probe into such a core on an increasingly smaller scale, molecular lines should have a symmetric velocity profile with a velocity width approaching the thermal velocity.

In a dense core undergoing inside-out collapse, the radial velocity depends on radius approximately as $r^{-0.5}$ (Shu 1977). As we probe into a *collapsing* core on an increasingly smaller scale, molecular lines should become *broader*. Zhou et al. (1993) noted that, for optically thick lines, the profiles should appear asymmetric, with stronger blue emission, and that the degree of asymmetry should increase with the optical depth of the line. This asymmetry is caused by the presence of two

[1] Astronomy Department, The University of Texas at Austin, Austin, TX 78712.
[2] MRAO, Cavendish Laboratory, University of Cambridge, Cambridge CB3 0HE, England.
[3] Astronomy Department, The University of Illinois, Urbana, IL 61801.
[4] Institute for Astronomy and Astrophysics, Academica Sinica, P.O. Box 1-87, Nankang, Taipei, Taiwan 115, R. O. C.
[5] Astronomy Department, Boston University, Boston, MA 02215.

points with the same projected velocity along any line of sight through the collapse region; as long as the molecular excitation temperature is decreasing with radius in the region where the velocity has a significant gradient, the blueshifted emission is always stronger than the redshifted emission for lines with substantial optical depth.

Lines with the properties just described can be formed in other ways, such as via cloud collisions (Keto & Lattanzio 1989) or cloud rotation (Adelson & Leung 1988) or, occasionally, in a general turbulent field (Falgarone et al. 1994). Observations of an optically thin line, as well as an optically thick one, are necessary to distinguish these causes from a possible collapse.

1.2. *Selection of Tracers*

Based on considerations of the collapse signatures, we chose the $C^{18}O$ $J = 2 \rightarrow 1$ line and the H_2CO $J_{K_{-1}K_1} = 3_{12} \rightarrow 2_{11}$ line as our tracers. The lowest two transitions of $C^{18}O$ are usually optically thin and easily detectable over a wide range of physical conditions (Myers, Link, & Benson 1983; Zhou et al. 1994b); they trace column density even at modest densities. We used the $J = 2 \rightarrow 1$ line of $C^{18}O$ to map globules, in order to locate regions of enhanced column density and measure their general properties, such as the radial velocity, average velocity width, column density distribution, and mass. In contrast, the H_2CO line is detectable only when high-density gas is present and is usually optically thick in the inner part of a typical dense core. Thus, H_2CO is useful to distinguish whether the column density enhancements traced by $C^{18}O$ are caused by density enhancements or by path-length enhancements.

The two lines are at similar frequencies and can be observed at the same telescope with similar beam sizes. $C^{18}O$ and H_2CO also have the same molecular weight and, hence, the same amount of thermal line broadening. In quiescent cores, the H_2CO line should have the same velocity centroid and similar or smaller line width than the $C^{18}O$ line; in collapsing cores, the H_2CO line, arising from the inner, denser collapsing regions, should be wider and asymmetric, with stronger blueshifted emission when viewed with adequate spatial and spectral resolution. We will identify candidates for collapse based on these spectral characteristics. The required resolution depends on several factors. We used a Monte Carlo code (Choi et al. 1995) to model the H_2CO line from collapsing clouds. With abundances large enough to make the line sufficiently opaque, an asymmetry is clearly visible if the diameter of the infall region is at least half the beam size. With a good signal-to-noise ratio (greater than 10:1), a collapsing region with a radius as small as one-quarter of the beam diameter can be detected. For a typical distance of 600 pc (CB), our 30″ beam limits us to sources with infall radii of at least 0.02 pc. For an effective sound speed such as that inferred for B335 (0.23 km s^{-1}), this radius would be reached in 9×10^4 yr, and a spectral resolution of 0.2 km s^{-1} is needed to resolve the two peaks. This relatively advanced age implies that most candidates would have substantial infrared emission from accretion onto the forming stellar core.

2. OBSERVATIONS

2.1. *Sample Selection*

Because our primary goal was to find evidence of collapse in simple molecular clouds, we chose a sample with the highest likelihood of showing collapse, one with evidence of ongoing star formation. As a result, our sample is not representative of all globules. However, a small number of globules without evidence of star formation were chosen as a control sample.

Yun & Clemens (1992; hereafter YC) list 39 positions of *IRAS* sources in 36 globules. The sources had been found either in the Point Source Catalog (PSC) or by analysis of *IRAS* co-added images. In addition, there is an *IRAS* source in CB 68, though it was not listed by YC, yielding 40 possible sources. We were able to observe 35 of these sources in 33 globules. All 14 outflow sources detected by YC were included in our sample. Five globules without known *IRAS* sources were chosen for the control sample. One (CB 12) was drawn from the control sample of YC and the other four (CB 44, CB 82, CB 231, and CB 233) from Leung et al. (1982), who found them to be unstable against gravitational collapse.

Table 1 lists the positions of 40 "targets," consisting of 35 *IRAS* sources and five globules without *IRAS* sources. Throughout this paper, CB source names will be used; other common names, with "B" from Barnard's catalog (1927), "L" from Lynds's Dark Nebula Catalog (Lynds 1962), and "LBN" from the Bright Nebula Catalog (Lynds 1965), can be found in Table 1. For sources with *IRAS* emission, the (0, 0) positions are the *IRAS* positions, taken either from the PSC or from the analysis by YC of the *IRAS* co-added images. For globules with no *IRAS* emission, the (0, 0) positions are approximately the maxima of visual extinction determined from the Palomar Observatory Sky Survey prints (CB).

2.2. *Data Collection*

The 10.4 m telescope of the Caltech Submillimeter Observatory (CSO),[6] on Mauna Kea, Hawaii, was used for all observations. The data were taken during observing runs in 1992 July, 1992 December, 1993 February, 1993 December, 1994 March, 1994 June, and 1995 March.

Observations were carried out in two stages. In the first stage, sources were initially surveyed at their (0, 0) positions in the $C^{18}O$ $J = 2 \rightarrow 1$ line (219.5603568 GHz; Winnewisser, Winnewisser, & Winnewisser 1985), followed by $C^{18}O$ mapping to locate the emission peak. In the second stage, observations toward the $C^{18}O$ peaks were performed in the H_2CO $J_{K_{-1}K_1} = 3_{12} \rightarrow 2_{11}$ line (225.697775 GHz; Lovas 1986). For cores that were initially not detected in $C^{18}O$ at the (0, 0) position, we mapped the ^{13}CO $J = 2 \rightarrow 1$ line (220.3986765 GHz; Winnewisser et al. 1985) to locate column density peaks.

The sources were observed by switching between the source position and a reference position 10′ westward. Telescope pointing was checked once every 2–3 hr each night by observing planets and found to be better than 6″ (rms). The beam size was 30″ (FWHM) at 230 GHz.

The standard chopper-wheel calibration procedure (Penzias & Burrus 1973) was used during the observations. The resulting antenna temperature, T_A^*, was corrected for atmospheric opacity and antenna rear spillover and scattering. The atmospheric opacity at 225 GHz toward the zenith ranged from 0.05 to 0.2 during these observations. The telescope main-beam efficiency (η_{mb}) at the time of the observations, 0.71 (Mangum 1993), can be used to convert T_A^* to main-beam radiation temperature, $T_{mb} = T_A^*/\eta_{mb}$. For a source that uniformly fills the main diffraction beam, T_{mb} is equivalent to T_R, in the notation of Kutner & Ulich (1981), if there is no signifi-

[6] The CSO is operated by the California Institute of Technology under funding from the National Science Foundation, contract AST 90-15755.

TABLE 1

BOK GLOBULE POSITIONS FOR $C^{18}O$ SURVEY

Source	Other Names	R.A. (1950)	Decl. (1950)	v_{LSR} (km s^{-1})	*IRAS* Point Source? (Y/N)
CB 3	LBN 594	$00^h25^m59^s$	56°25′32″	−38.4	Y[a]
CB 6	LBN 613	00 46 34	50 28 25	−12.4	Y
CB 12	...	01 35 05	64 50 00	−11.4	N
CB 13	L1345	01 53 16	62 31 36	35.9	Y
CB 28	LBN 923	05 03 45	−04 02 58	8.5	Y
CB 29	...	05 19 28	−03 43 26	11.2	Y
CB 30	...	05 26 52	05 38 15	−0.1	Y
CB 32	LBN 921	05 33 48	−00 19 05	−5.0	Y
CB 34	...	05 44 03	20 59 07	0.5	Y[a]
CB 39	...	05 59 06	16 30 58	2.4	Y[a]
CB 44	B227, L1570	06 04 34	19 28 19	−0.3	N
CB 50	...	06 31 36	07 49 10	1.0	Y
CB 52	...	06 46 25	−16 50 38	16.8	Y
CB 54	LBN 1042	07 02 06	−16 18 47	19.7	Y[a]
CB 58-1	...	07 15 56	−23 29 36	15.1	Y
CB 58-2	...	07 16 09	−23 36 11	15.1	Y
CB 68	L146	16 54 24	−16 04 45	5.5	Y
CB 81	L1774	17 19 19	−27 05 20	3.7	Y[a]
CB 82	B68, L55	17 19 34	−23 47 45	3.4	N
CB 142	...	18 27 10	−13 42 51	18.6	Y
CB 170	B127, L544	18 58 44	−05 33 40	10.2	Y
CB 171	B128	18 59 12	−04 38 17	16.7	Y
CB 175	B129, L549	18 59 20	−05 22 38	10.0	Y
CB 180	B133, L531	19 03 35	−06 56 38	11.6	Y
CB 188	...	19 17 57	11 30 18	6.8	Y[a]
CB 203	...	19 41 42	18 58 27	14.6	Y
CB 205	L810	19 43 22	27 44 01	15.3	Y[a]
CB 206	L758	19 44 23	18 57 49	15.2	Y
CB 214	L814	20 01 54	26 29 42	9.1	Y[a]
CB 216	L797	20 03 45	23 18 25	12.5	Y[a]
CB 217	L863	20 05 55	36 48 14	−2.1	Y[a]
CB 230	L1177	21 16 55	68 04 52	2.7	Y[a]
CB 231	B157	21 32 18	54 28 06	6.5	N
CB 232	B158	21 35 14	43 07 05	12.5	Y[a]
CB 233	B161	21 39 00	57 34 26	−0.8	N
CB 240-1	L1192	22 31 46	58 16 26	−3.9	Y
CB 240-2	...	22 32 08	58 18 28	−3.9	Y
CB 243	L1246	23 22 53	63 20 04	−11.3	Y
CB 244	L1262	23 23 49	74 01 08	4.2	Y[a]
CB 247	L1263	23 55 04	64 30 10	−3.7	Y[a]

[a] Outflow sources detected by Yun & Clemens 1992.

cant coupling of the sidelobes to the source. Most of the sources are more extended in the $C^{18}O$ maps than the size of the main diffraction beam and the nearest sidelobes; thus, using T_{mb} likely overestimates T_R. The efficiency correction for telescope forward spillover and scattering, η_{fss}, measured on the Moon, is 17% larger than η_{mb} ($\eta_{fss} = 0.83$; Mangum 1993), so the overestimation should be less than 20% for these globules. The facility's 230 GHz SIS receiver operated in double-sideband mode. Considering all sources of uncertainties, including uncertainties in the sideband gain ratio, an overall uncertainty of 20% for T_{mb} is likely.

The back end was an acousto-optic spectrometer (AOS) with 1024 channels operating over a bandwidth of 50 MHz. The data were smoothed by two channels, with a resultant channel separation of 97 kHz, or 0.13 km s^{-1}. The FWHM velocity resolution was measured by injection of a monofrequency signal at the AOS input and found to be 153 ± 10 kHz (0.20 ± 0.02 km s^{-1}) in 1994 June, 137 ± 20 kHz (0.18 ± 0.03 km s^{-1}) in 1995 March, and 127 ± 17 kHz (0.17 ± 0.02 km s^{-1}) on all other runs. Typical rms noise after smoothing was 0.1 K in T_A^*.

For the data taken between 1993 February and 1994 March, there were shifts of 0.1–0.3 km s^{-1} in line centroids between spectra taken toward the same position on different nights (see also Zhou et al. 1994b). There were no velocity shifts larger than one AOS resolution element among spectra taken on the same night. More than half of the data presented in this paper were obtained in 1992 July and were not obviously affected by this uncertainty in velocity. The source of the velocity shifts has not been fully determined, but the most likely source is inadequate accuracy in the program used to calculate Doppler shifts due to the Earth's motion and send frequencies to a synthesizer. This problem was solved for the 1995 March run, when spectra were obtained for CB 54.

3. RESULTS

3.1. $C^{18}O$ *Survey*

Of the 40 targets in the sample, 27 (70%) were detected at 3 σ or better in the $C^{18}O$ line; there were also three marginal detections (~3 σ). Four of the five globules in the control sample were detected. The upper limits toward the remaining 10 targets are typically 0.2 K (2 σ). We mapped 26 of the detected globules, including all sources with $T_A^* \gtrsim 0.5$ K, over at least nine positions, with 30″ spacing; we were able to locate $C^{18}O$ emission maxima in 20 globules, including 18 with *IRAS*

sources and two without *IRAS* sources (CB 12 and CB 82). Parameters of the $C^{18}O$ $J = 2 \rightarrow 1$ line at the positions of the peaks of T_A^* are summarized in Table 2, including the position offsets ($\Delta\alpha$ and $\Delta\delta$) of the peaks from the positions in Table 1. The peak T_A^*, line velocity, intrinsic FWHM line width (corrected for instrumental broadening), integrated line intensity, and rms noise, all listed in Table 2, were determined from Gaussian line fits. The uncertainties from the fits are given in parentheses. Upper limits (2 σ) are given for the 10 globules that were not clearly detected, nine of which contained an *IRAS* source. Four of these nine *IRAS* sources were detected only in co-added images; all five that appear in the PSC have cirrus flags high enough to cause concern. For example, the CIRR1 flags range from 5 to 9, where values exceeding 3 indicate possible problems (Beichman et al. 1987). These sources may not be self-luminous, though one (CB 39) is associated with an outflow and a near-infrared source (Yun 1993).

Four globules not detected in $C^{18}O$ were mapped in the $J = 2 \rightarrow 1$ line of ^{13}CO to ascertain whether there was a nearby peak. One (CB 13) was not detected in ^{13}CO; the other three were reobserved in $C^{18}O$ at the ^{13}CO peak but not detected. In addition, two sources with weak $C^{18}O$ detections were observed in ^{13}CO. These sources are discussed in § 4.1.

3.2. $C^{18}O$ *Maps*

For the 12 sources in which the $C^{18}O$ maps extended to the half-maximum of the local peaks in the integrated intensity, Figures 1*a*–1*f* show the integrated intensity maps, with the locations of *IRAS* sources marked as filled squares. Eleven of these 12 globules have well-defined spatial peaks in their $C^{18}O$ distributions. Five of them have a single, dominant peak. CB 82, a globule from the control sample, is the only mapped globule with no well-defined spatial peak in the $C^{18}O$ emission, although it appears rather compact and opaque in the optical.

Given the 30″ spacing and beam size of the $C^{18}O$ maps and the uncertainties in the *IRAS* positions (typically 15″), we consider the source to be associated with the $C^{18}O$ peak if the two coincide within 34″, the quadrature sum of the two uncertainties. Of the 18 mapped globules with clear peaks and *IRAS*

TABLE 2

$C^{18}O$ $J = 2 \rightarrow 1$ RESULTS

Source	Number of Points	Peak[a] Position	T_A^* (K)	V_{LSR} (km s^{-1})	Δv[b] (FWHM) (km s^{-1})	$\int T_A^* dv$ (K km s^{-1})	rms Noise (K)	N_{H_2} (10^{21} cm^{-2})
CB 3	32	(−30″, 0″)	2.4	−38.5(0.01)	1.6(0.03)	4.1(0.07)	0.09	29
CB 6	15	(0, 0)	1.3	−12.4(0.01)	0.6(0.03)	0.8(0.03)	0.07	5.8
CB 12	9	(0, 0)	1.9	−11.4(0.01)	0.9(0.03)	1.8(0.05)	0.1	12
CB 13	1	(0, 0)	<0.2	...	...	...	0.1	...
CB 28	3	(−30, 90)	0.4	8.5(0.09)	1.4(0.19)	0.6(0.07)	0.1	3.9
CB 29	10	(90, 0)	<0.2	...	...	...	0.1	...
CB 30	9	(0, 0)	<0.1	...	...	...	0.05	...
CB 32	13	(120, −30)	1.1	−5.0(0.01)	0.7(0.03)	0.9(0.03)	0.07	5.5
CB 34	14	(0, 0)	0.6	0.5(0.04)	1.5(0.08)	1.0(0.05)	0.07	9.9
CB 39	9	(0, 0)	<0.2	...	...	...	0.07	...
CB 44	9	(−30, 30)	0.7	−0.3(0.05)	0.8(0.10)	0.6(0.08)	0.1	5.2
CB 50	9	(30, 30)	0.3	0.9(0.04)	0.5(0.12)	0.1(0.03)	0.06	3.0
CB 52	9	(0, 0)	0.5	16.8(0.06)	1.0(0.12)	0.6(0.06)	0.1	4.6
CB 54	18	(0, 0)	1.6	19.6(0.01)	1.4(0.03)	2.5(0.05)	0.06	17
CB 58-1	1	(0, 0)	<0.4	...	...	...	0.2	...
CB 58-2	8	(0, 0)	1.2	15.1(0.03)	0.9(0.08)	1.2(0.09)	0.2	7.9
CB 68	36	(60, 0)	1.1	5.2(0.02)	0.8(0.03)	0.9(0.04)	0.1	6.0
CB 81	9	(0, −30)	~0.3	3.7(0.05)	0.3(0.09)	0.1(0.03)	0.1	2.9
CB 82	25	(60, 0)	1.0	3.4(0.02)	0.4(0.06)	0.4(0.05)	0.1	3.8
CB 142	9	(−30, −30)	0.4	18.6(0.06)	0.7(0.17)	0.3(0.05)	0.08	3.8
CB 170	9	(0, 0)	0.4	10.2(0.04)	0.3(0.11)	0.1(0.03)	0.1	3.4
CB 171	9	(0, 0)	<0.2	...	...	...	0.1	...
CB 175	1	(0, 0)	~0.3	10.0(0.05)	0.4(0.20)	0.2(0.05)	0.1	3.8
CB 180	1	(0, 0)	0.4	11.6(0.06)	0.7(0.13)	0.3(0.05)	0.1	3.8
CB 188	20	(−30, 0)	0.9	6.8(0.04)	1.0(0.09)	0.7(0.06)	0.1	6.0
CB 203	9	(30, −30)	<0.2	14.4(0.04)	...	0.1(0.03)	0.1	...
CB 205	25	(0, −30)	1.1	15.3(0.04)	2.3(0.10)	2.7(0.09)	0.1	17
CB 206	1	(0, 0)	<0.2	...	...	...	0.1	...
CB 214	1	(0, 0)	0.4	9.1(0.06)	0.6(0.16)	0.3(0.05)	0.1	4.3
CB 216	14	(0, −30)	1.3	12.5(0.02)	1.1(0.06)	1.6(0.06)	0.1	14
CB 217	9	(−30, −30)	0.6	−2.1(0.04)	0.3(0.10)	0.2(0.05)	0.1	3.8
CB 230	15	(0, 0)	1.2	2.7(0.01)	0.8(0.03)	0.8(0.03)	0.05	8.4
CB 231	1	(0, 0)	<0.2	6.5	0.4	0.1	0.1	...
CB 232	39	(0, 0)	0.8	12.4(0.03)	1.0(0.04)	0.9(0.02)	0.05	6.7
CB 233	1	(0, 0)	0.4	−0.8(0.03)	0.5(0.08)	0.2(0.03)	0.06	3.8
CB 240-1	1	(0, 0)	0.4	−3.9(0.04)	0.3(0.09)	0.1(0.03)	0.1	3.2
CB 240-2	1	(0, 0)	<0.2	...	...	...	0.08	...
CB 243	1	(0, 0)	0.5	−11.4(0.06)	0.9(0.13)	0.5(0.06)	0.1	3.8
CB 244	39	(0, 0)	1.7	4.1(0.01)	0.7(0.02)	1.3(0.02)	0.07	9.2
CB 247	5	(0, 0)	~0.2	−4.0(0.10)	1.0(0.17)	0.2(0.03)	0.07	3.8

[a] Offsets of local peaks in arcseconds.

[b] An instrumental broadening of 0.15 km s^{-1} has been removed from the observed line width.

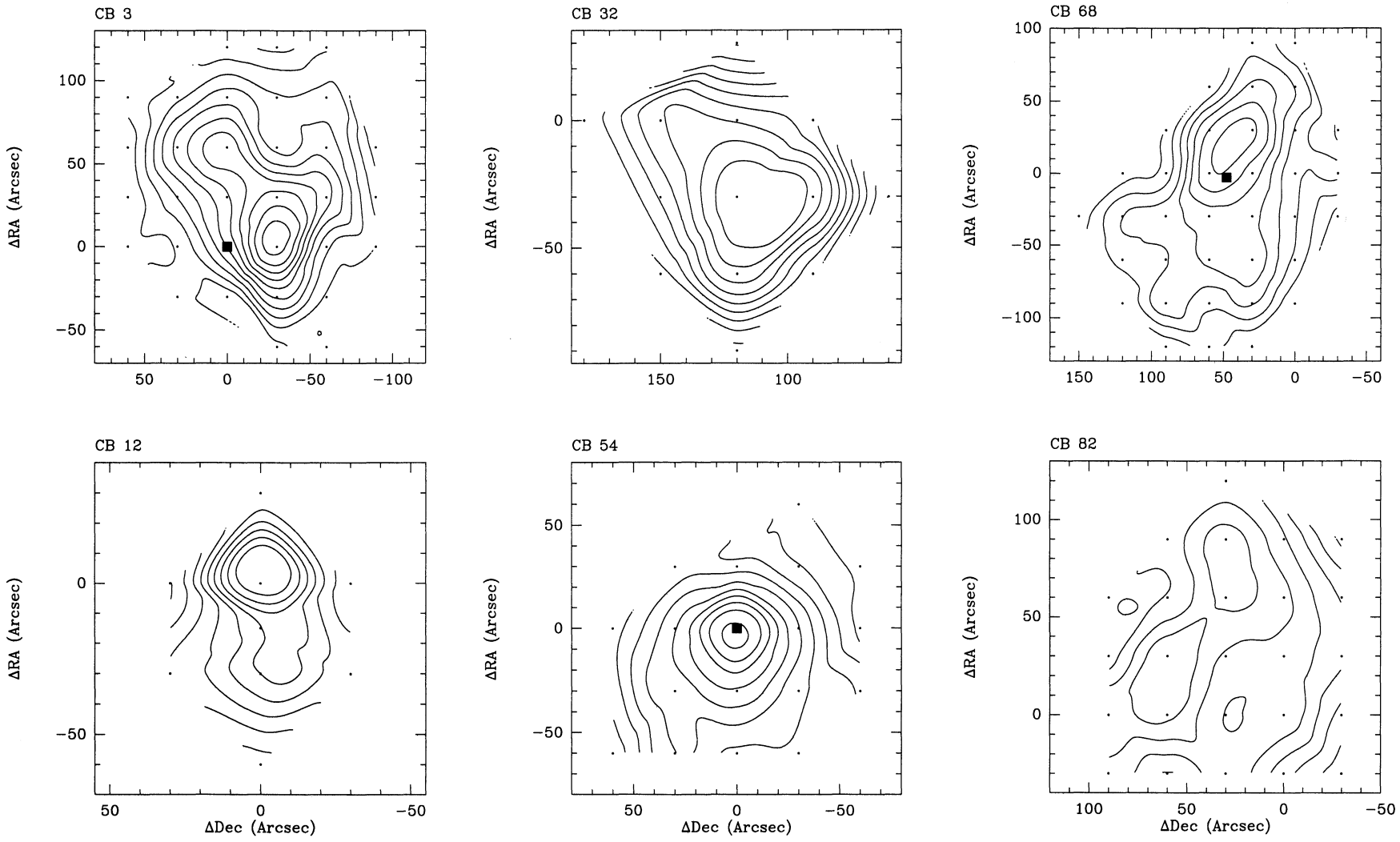

FIG. 1a FIG. 1b FIG. 1c

FIG. 1.—Maps of $C^{18}O$ $J = 2 \rightarrow 1$ integrated intensity. The first contours are 3 σ and the spacings are either 3 or 2 σ. The positions of the *IRAS* point sources are indicated by squares. (*a*) CB 3 and CB 12. The first contours and the contour spacings are 0.4 and 0.14 K km s^{-1} for CB 3 and CB 12, respectively. (*b*) CB 32 and CB 54. The first contours and the contour spacings are 0.08 and 0.18 K km s^{-1} for CB 32 and CB 54, respectively. (*c*) CB 68 and CB 82. The first contours and the contour spacings are 0.12 and 0.06 K km s^{-1} for CB 68 and CB 82, respectively. (*d*) CB 188 and CB 205. The first contours and the contour spacings are 0.12 and 0.22 K km s^{-1} for CB 188 and CB 205, respectively. (*e*) CB 216 and CB 230. The first contours and contour spacings are 0.16 and 0.07 K km s^{-1} for CB 216 and CB 230, respectively. (*f*) CB 232 and CB 244. The first contours and the contour spacings are 0.16 and 0.13 K km s^{-1} for CB 232 and CB 244, respectively. The contours around (0, 50) in the CB 244 map enclose a minimum of emission; the emission is rising again at the northeast and northwest boundaries of the map.

1995ApJ...454..217W

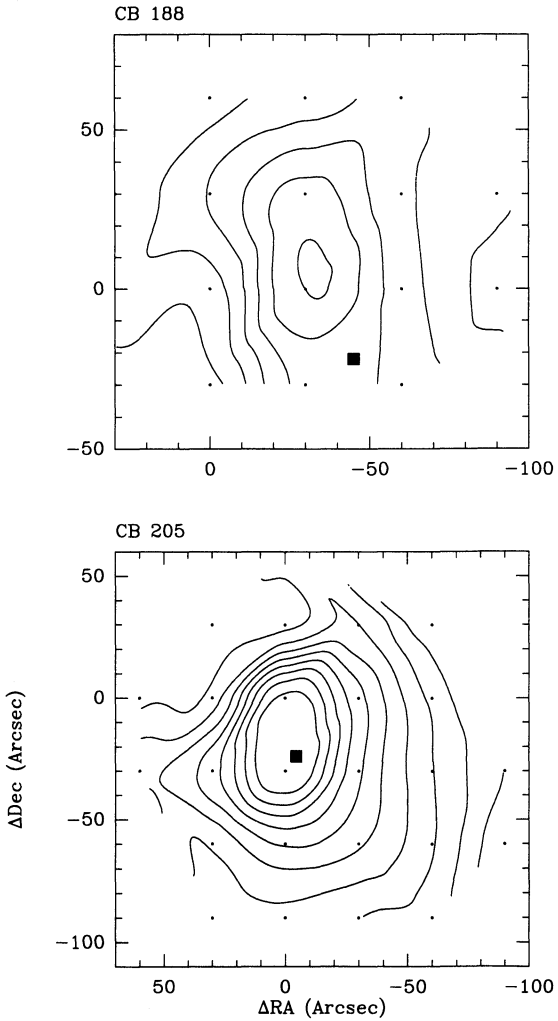

FIG. 1*d*

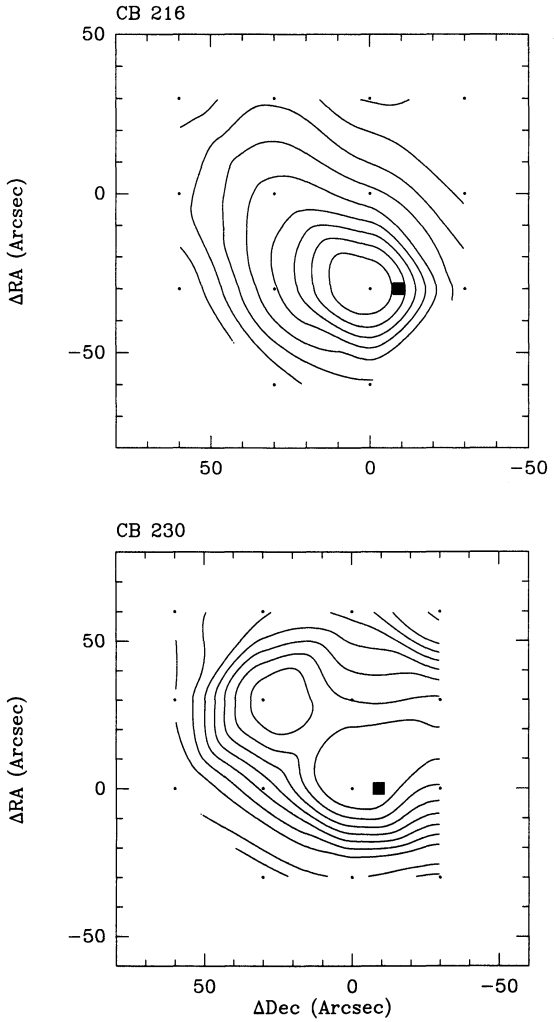

FIG. 1*e*

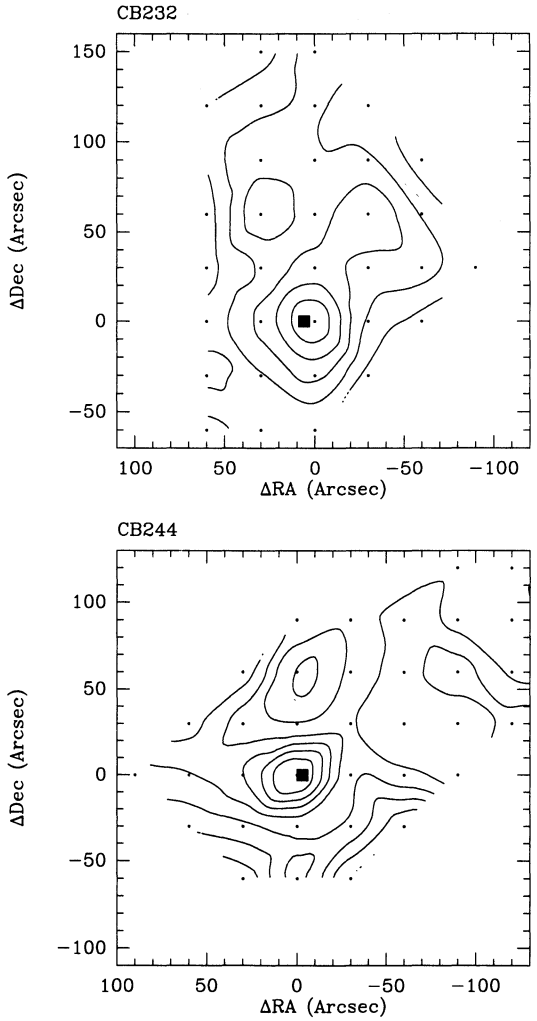

FIG. 1*f*

sources, 12 meet this criterion, four peaks are more than 60″ from the nearest *IRAS* source, and two peaks lie between 34″ and 60″ from the nearest *IRAS* source.

3.3. $H_2CO\ 3_{12} \rightarrow 2_{11}$ *Survey*

We detected the $H_2CO\ 3_{12} \rightarrow 2_{11}$ line toward peaks of the $C^{18}O\ J = 2 \rightarrow 1$ emission in nine of the 12 globules with *IRAS* sources within 34″ and toward two of the three peaks in globules without a nearby *IRAS* source (see Table 3). Figure 2 shows the H_2CO and $C^{18}O$ line profiles. The line widths of the H_2CO line are significantly wider than those of the $C^{18}O$ line in three globules (CB 3, CB 54, and CB 244). In profiles with two velocity peaks (e.g., CB 3 and CB 244), the line width refers to the best-fit Gaussian profile, which usually ignores the narrow peaks. The line widths of the H_2CO lines are much narrower (and less than or equal to the width of the $C^{18}O$ lines) at positions displaced from the peak for these three globules (Figs. 2*a*–2*c*).

4. PHYSICAL PARAMETERS

In this section, we discuss the physical parameters of the cloud cores based on an analysis of the $C^{18}O$ and H_2CO observations. The $C^{18}O$ data were used to derive the column density, mass, and mean density. The H_2CO line strength was used to constrain the volume density.

4.1. *Column Density*

The $C^{18}O$ column density was calculated from the expression (see Choi, Evans, & Jaffe 1993)

$$N(C^{18}O) = 9.91 \times 10^{14}\ \mathrm{cm}^{-2} \times \frac{\int T_{mb}(C^{18}O)\,dv}{D(n, T_K)} \frac{\tau_{21}}{1 - \exp(-\tau_{21})}, \quad (1)$$

where $\int T_{mb}(C^{18}O)\,dv$ is the integrated intensity of the $C^{18}O$ $J = 2 \rightarrow 1$ line in units of K km s^{-1}, τ_{21} is the peak optical depth of the line, and $D(n, T_K)$ is given by

$$D(n, T_K) = f_1[J(T_{ex}) - J(T_{bg})](1 - e^{-10.5/T_{ex}}). \quad (2)$$

$J(T)$ is the Planck function in temperature units, f_1 is the fraction of the total abundance found in the $J = 1$ level, T_{ex} is the excitation temperature, and $T_{bg}(= 2.8\ \mathrm{K})$ is the temperature of the cosmic background.

The optical depth, τ_{21}, was estimated from the ratio of the line temperatures of the $^{12}CO\ J = 2 \rightarrow 1$ (taken from CB) and $C^{18}O\ J = 2 \rightarrow 1$ lines by assuming that the ^{12}CO line is completely opaque and has the same excitation temperature as the $C^{18}O$ line. The calculated τ_{21} ranges from $\lesssim 0.04$ to 0.8. The fact that the $^{12}CO\ J = 2 \rightarrow 1$ line was observed using a different telescope (70″ beam) is unlikely to cause serious errors in τ_{21} since $^{12}CO\ J = 2 \rightarrow 1$ emission is likely to be much more extended than the $C^{18}O$ emission, so the correction due to different source couplings is small. The main uncertainty in τ_{21} arises from the assumption of equal excitation temperatures. However, since most clouds in our sample are only moderately opaque in $C^{18}O$, with $\tau < 0.4$, the correction for column density due to line opacity (the last term in eq. [1]) is insignificant ($\lesssim 20\%$) for most globules.

The unknowns in $D(n, T_K)$ are f_1 and T_{ex}, which both depend on density (n) and temperature (T_K). The usual assumptions made to derive column density (collectively known as the LTE approximation) are that the density is large enough to allow radiative decays from all levels to be neglected, that the temperature in the region forming the $C^{18}O$ line can be calculated from the ^{12}CO line, and that the temperature is much greater than hB/k, where B is the rotation constant. The LTE approximation can be in error in a number of ways: it overestimates the column density for hot gas at modest density (Choi et al. 1993); for cold gas, it underestimates the column density (Zhou et al. 1994b). To check the LTE assumption, we made sta-

TABLE 3

$H_2CO\ 3_{21} \rightarrow 2_{11}$ RESULTS

Source	Offset	T_A^* (K)	rms Noise (K)	v_{LSR} (km s^{-1})	Δv (km s^{-1})	$\frac{T_A^*(H_2CO)}{T_A^*(C^{18}O)}$	$\frac{\Delta v(H_2CO)}{\Delta v(C^{18}O)}$
Cores with *IRAS* Point Sources							
CB 3	(−30″, 0″)	0.34[a]	0.04	−38.6(0.08)	8.37(0.22)	0.14(0.02)	5.2(0.17)
	(0, 60)	0.16	0.04	−38.1(0.04)	0.5(0.09)	0.07(0.02)	0.4(0.10)
CB 6	(0, 0)	0.07	0.02	−12.3(0.02)	0.8(0.23)	0.05(0.02)	1.3(0.39)
CB 34	(0, 0)	0.30	0.07	0.4(0.03)	1.5(0.08)	0.5(0.13)	1.0(0.07)
CB 52	(0, 0)	<0.1	0.05	...	...	...	...
CB 54	(0, 0)	0.68	0.03	19.4(0.03)	2.5(0.07)	0.4(0.03)	1.8(0.06)
	(0, −60)	0.16	0.05	19.9(0.05)	0.5(0.1)	0.2(0.07)	0.4(0.1)
CB 68	(60, 0)	0.24	0.02	5.1(0.02)	0.4(0.05)	0.2(0.02)	0.5(0.07)
CB 188.....	(−30, −30)	<0.06	0.02	...	...	...	...
CB 205.....	(0, −30)	0.08	0.02	15.9(0.10)	1.5(0.29)	0.07(0.02)	0.7(0.13)
CB 216.....	(0, −30)	<0.05	0.02	...	...	...	...
CB 230.....	(0, 0)	0.36	0.03	2.8(0.01)	0.7(0.04)	0.3(0.03)	0.9(0.06)
CB 232.....	(0, 0)	0.14	0.02	12.6(0.05)	1.2(0.19)[b]	0.17(0.03)	1.2(0.20)
CB 244.....	(0, 0)	0.27	0.02	4.2(0.04)	1.9(0.09)	0.16(0.01)	2.7(0.15)
	(−150, 90)	0.19	0.05	4.3(0.04)	0.5(0.12)	0.12(0.03)	0.9(0.19)
Cores without *IRAS* Point Sources							
CB 12	(0″, 0″)	0.13	0.03	−11.4(0.06)	0.7(0.12)	0.07(0.02)	0.8(0.14)
CB 32	(120, −30)	<0.1	0.04	...	...	...	...
CB 82	(60, 0)	0.08	0.02	3.5(0.04)	0.3(0.10)	0.08(0.02)	0.8(0.27)

[a] The Gaussian fit includes, but mostly ignores, the narrow blue peak.
[b] The Gaussian fit excludes the red shoulder.

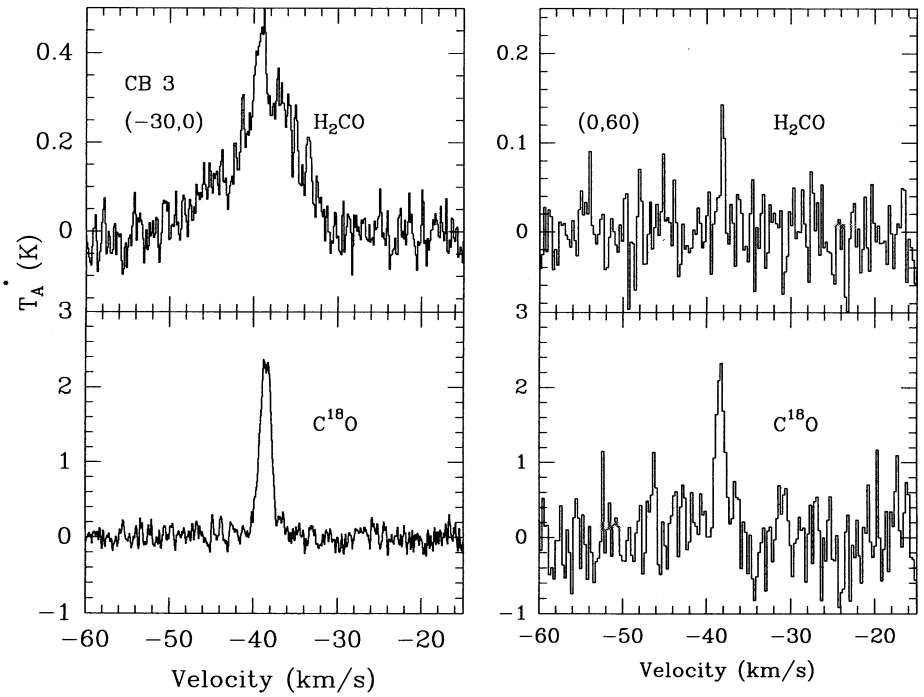

FIG. 2a

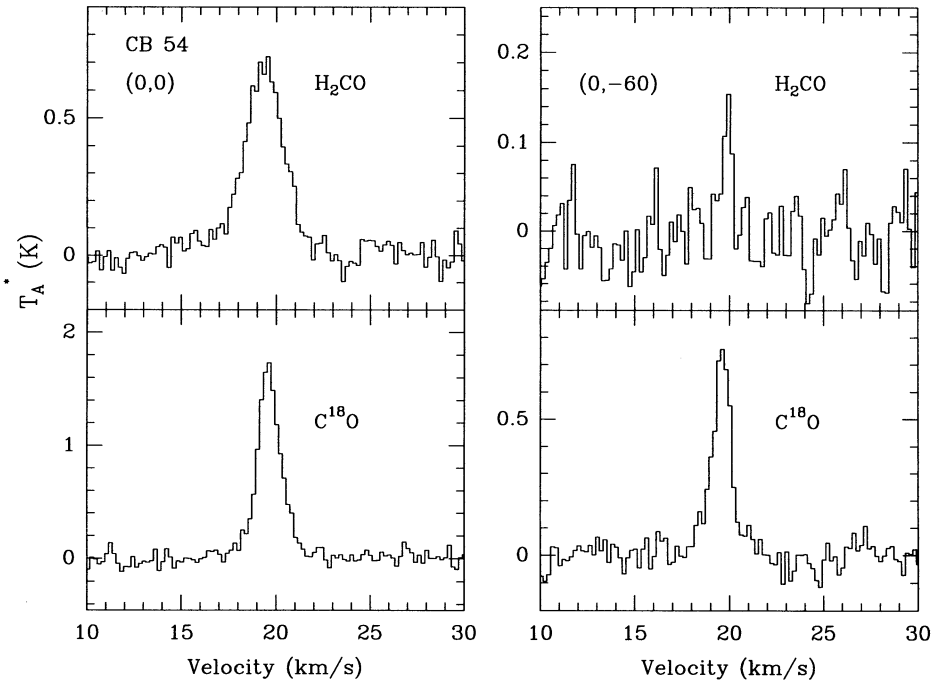

FIG. 2b

FIG. 2.—Profiles of the H_2CO $J_{K_{-1}K_1} = 3_{12} \rightarrow 2_{11}$ and $C^{18}O$ $J = 2 \rightarrow 1$ lines in all the globules with H_2CO detections. The temperature scales are in T_A^* units. (*a*) CB 3 spectra at the peak of $C^{18}O$ emission (−30, 0) and at a position well away from the peak (0, 60). (*b*) CB 54 spectra toward the peak (0, 0) and well away from the peak (0, −60). (*c*) CB 244 spectra toward the peak (0, 0) and well away from the peak (−150, 90). (*d*) CB 12, CB 82, and CB 6 spectra toward the peaks. (*e*) CB 54, CB 34, and CB 230 spectra toward the peaks. (*f*) CB 68, CB 205, and CB 232 spectra toward the peaks.

tistical equilibrium calculations using both the large velocity gradient (LVG) model (de Jong, Chu, & Dalgarno 1975) and a microturbulent model using a Monte Carlo code (Choi et al. 1995). The results indicate that the LTE method always underestimates the column density for finite density and temperatures in the range found for these globules ($T_K = 10.6 \pm 2.7$ K) from the data of CB. However, for the typical densities derived later in the paper ($n \gtrsim 10^4$ cm^{-3}), the effect is small (about 6%). Consequently, we used the LTE approximation to $D(n, T_K)$; we set $T_{ex} = T_K$ and

$$f_1 = \frac{3}{Z} e^{-5.25/T_K}, \quad Z = \frac{k}{hB}\left(T_K + \frac{hB}{3k}\right). \tag{3}$$

The derived $C^{18}O$ column densities span a range from

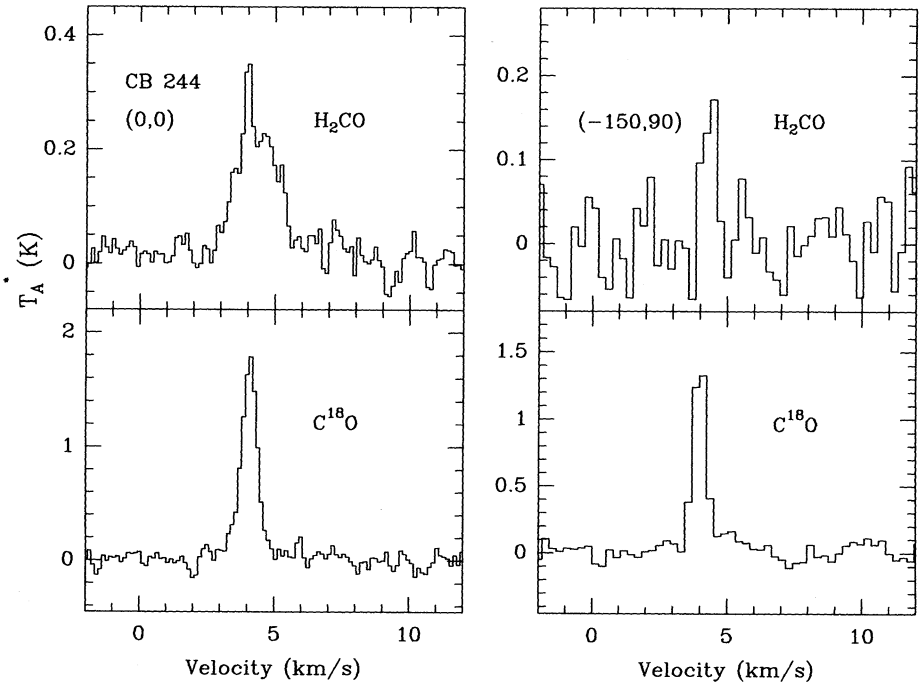

FIG. 2c

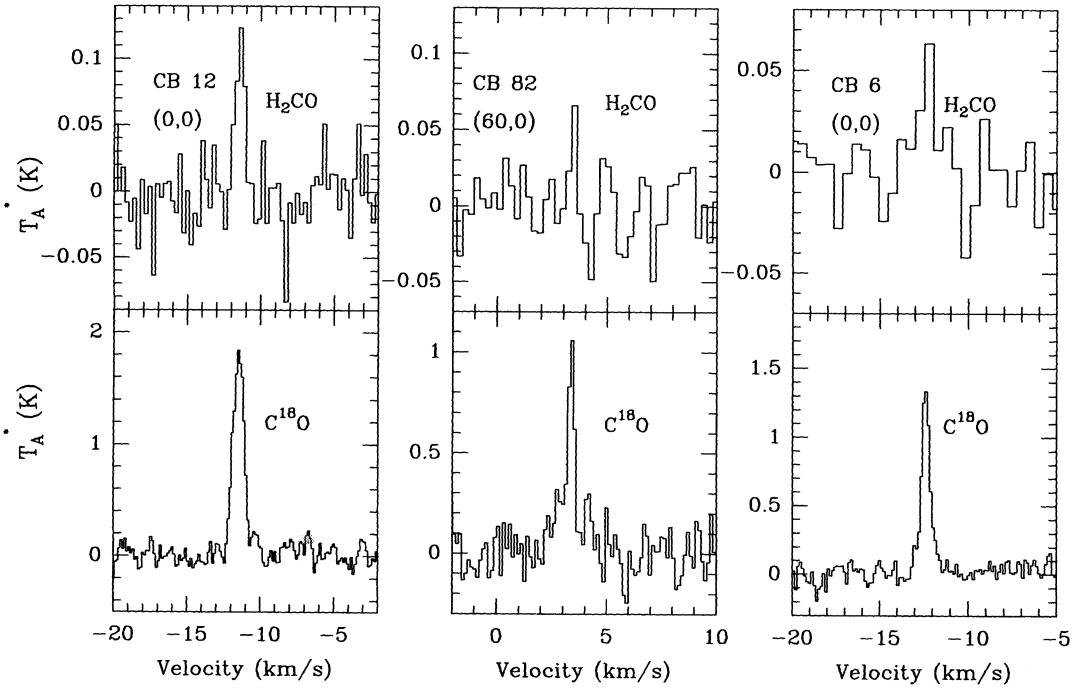

FIG. 2d

8×10^{13} cm^{-2} to 5×10^{15} cm^{-2}. The corresponding range of visual extinction is 3–30 mag, obtained from the relations between $C^{18}O$ column density and visual extinction derived by Frerking, Langer, & Wilson (1982): $A_V = 5.88 \times 10^{-15} N(C^{18}O) + 1.3$ for $A_V > 4$, and $A_V = 1.42 \times 10^{-14} N(C^{18}O) + 1.9$ for $A_V < 4$. The range of A_V is less than that of the $C^{18}O$ column density because the relationship between A_V and $N(C^{18}O)$ changes for $A_V < 4$ mag and because of a constant A_V term in the relationship. The nature of the different relationships causes a substantial number of globules to appear to have the same A_V (4 mag). From the derived A_V and the relation $N_{H_2} = 9.4 \times 10^{20} A_V$, we calculated the H_2 column densities listed in Table 2. Similar relations between A_V and $N(C^{18}O)$ were found by Cernicharo & Guélin (1987) [$\sim$30% lower A_V for the same $N(C^{18}O)$] and by Nozawa et al. (1991), who found a larger constant A_V term. The differences between

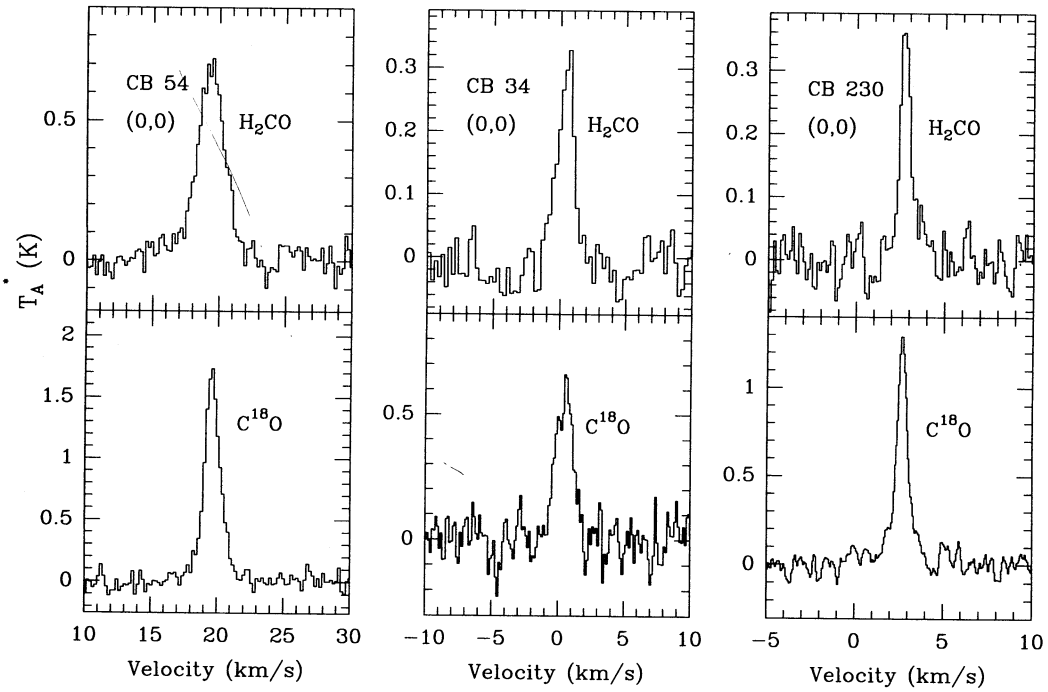

FIG. 2e

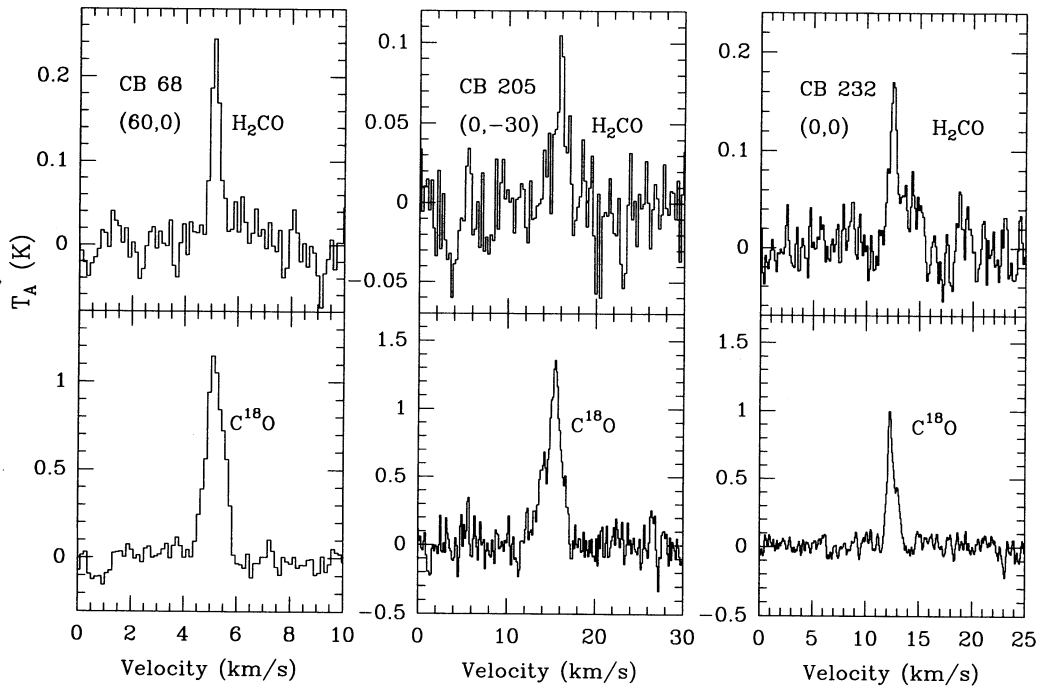

FIG. 2f

authors are small except at low A_V, where they are all very uncertain.

Values of N_{H_2} less than 5×10^{21} cm^{-2} should be viewed with caution, since they correspond to the A_V near the change in relationships from Frerking et al. (1982). Furthermore, the globules without $C^{18}O$ detections raise questions about the use of $C^{18}O$ to estimate A_V. The ratio of T_A^* for $^{13}CO/C^{18}O$ exceeds 18 for some globules, much greater than the terrestrial isotopic ratio of 5.6. Turner (1994a) has also found high ratios in some globules without infrared sources; he found that isotope-selective photodissociation and fractionation of ^{13}C (see van Dishoeck & Black 1988) could explain most of his results. If a similar explanation applies to the globules with high ratios in our sample, then some of the low column densities in Table 2 will be underestimations. However, globules with $C^{18}O$ lines strong enough to map are unlikely to have low

$C^{18}O/^{13}CO$ ratios (see Table 1 of Turner 1994a), so the masses and mean densities computed in the following sections are probably not strongly affected.

4.2. *Mass*

For sources mapped in the $C^{18}O$ $J = 2 \rightarrow 1$ line beyond their half-maximum intensities, the masses (denoted M_N) were estimated from the column densities as

$$M_N = \mu m_H N_{H_2} \Delta\Omega d^2 , \quad (4)$$

where $\Delta\Omega = (\pi/4)\Delta\theta_1 \Delta\theta_2$, where $\Delta\theta_1$ and $\Delta\theta_2$ are the deconvolved, FWHM sizes along the major and minor axes (Table 4), and d is the distance.

Mass was also estimated using the virial theorem:

$$M_V = \frac{5\Delta\theta v_{rms}^2 d}{3G} , \quad (5)$$

where $\Delta\theta = \sqrt{\Delta\theta_1 \Delta\theta_2}$, $v_{rms} = \Delta v/2.35$, and Δv is the FWHM line width, measured at quiescent positions located away from the emission peaks.

The distances to most of the globules in the sample are unknown. CB argued that the distances to most of the globules should be less than 1 kpc and suggested a mean distance of 600 pc. A nominal distance of 600 pc was assumed for all globules except CB 3 (Scappini, Caselli, & Palumbo 1991) and CB 205 (L810) (Turner 1986; Xie & Goldsmith 1990), for which we adopted distances of 2.5 kpc, and CB 244 (L1262), for which we adopted a distance of 200 pc (Myers et al. 1983). Since $M_N \propto d^2$ and $M_V \propto d$, M_V is probably more reliable.

Table 4 presents the sizes and masses; note that three globules (CB 6, CB 34, and CB 52) with H_2CO data in Table 3 do not appear in Table 4 because the $C^{18}O$ maps do not extend beyond the half-maximum contour. The derived masses (M_V) range from 0.8 to 7 $M_\odot$, leaving aside CB 3 and CB 205, which have much larger masses ($M_V = 67$ and 117 $M_\odot$, respectively).

4.3. *Volume Density*

The gas volume density was estimated with two methods: (1) division of the H_2 column density by the mean size of the $C^{18}O$ $J = 2 \rightarrow 1$ emission region; and (2) an excitation analysis of the H_2CO line. An average gas density ($\langle n \rangle$) along the line of sight is obtained using the first method, while H_2CO excitation analysis returns a volume density (n) characteristic of the region giving rise to the H_2CO emission. The latter will usually exceed the former if there are density variations along the line of sight.

The quantity $\langle n \rangle$ is given by

$$\langle n \rangle = \frac{N_{H_2}}{\Delta\theta d} . \quad (6)$$

The quantity n was estimated from models of the excitation of H_2CO by use of an LVG code. The kinetic temperature for each globule was derived from the ^{12}CO $J = 2 \rightarrow 1$ line intensity taken from CB. Since the $C^{18}O$ column density along the line of sight is already constrained by the integrated $C^{18}O$ line intensity, the H_2CO column density was calculated by assuming an H_2CO-to-$C^{18}O$ abundance ratio. Given the kinetic temperature and the H_2CO column density, the remaining variable (n) was found by matching the model and observed H_2CO line strengths. Turner (1994b) studied a sample of 27 CB globules in the 2 cm and 6 cm K-doublet lines and the $J = 2 \rightarrow 1$ line of H_2CO; he found $X(H_2CO)/X(C^{18}O)$ ranging from 1×10^{-2} to 7×10^{-2}. Using this range of the abundance ratio, we derived a range of volume densities, n. Note that the density derived through excitation analysis is independent of the distance of the globules but that derived from $C^{18}O$ is proportional to d^{-1}.

The average density (see Table 4) ranges from 7×10^3 to 7×10^4 cm^{-3}, while the H_2CO-traced density ranges from 1.5×10^4 to 2.2×10^6 cm^{-3}. The large range in the H_2CO-traced density for an individual source reflects the large range of possible $X(H_2CO)/X(C^{18}O)$ values. A second transition of

TABLE 4

DERIVED PROPERTIES OF CORES WITH H_2CO OBSERVATIONS

Source	Size[a]	M_N ($M_\odot$)	M_V ($M_\odot$)	$\langle n \rangle$[b] (cm^{-3})	n[c] (cm^{-3})
CB 3	95″ × 40″	230	67	1.3×10^4	1.8×10^5–1.7×10^6
CB 12	30 × 30	1.3	2.5	4.9×10^4	1.5×10^4–1.1×10^5
CB 32	55 × 50	1.9	2.6	1.2×10^4	$<2.6 \times 10^4$–1.8×10^5
CB 54	30 × 30	1.8	6.9	6.0×10^4	2.3×10^5–2.2×10^6
CB 68	120 × 45	3.9	4.8	9.1×10^3	3.6×10^4–2.5×10^5
CB 82	120 × 30	1.6	1.0	7.0×10^3	2.6×10^4–1.8×10^5
CB 188	75 × 30	1.6	4.9	1.4×10^4	$<4.0 \times 10^4$–2.3×10^5
CB 205	60 × 45	98	117	8.9×10^3	1.8×10^4–1.3×10^5
CB 216	40 × 30	2.0	4.3	4.4×10^4	$<1.3 \times 10^4$–9.1×10^4
CB 230	80 × 40	3.3	3.7	1.7×10^4	6.9×10^4–5.4×10^5
CB 232IR[a]	70 × 45	2.5	5.8	1.3×10^4	8.5×10^4–5.5×10^5
CB 244IR[d]	50 × 40	0.3	0.8	6.9×10^4	1.3×10^5–1.0×10^6
Av[e]	67 × 37	2.0	3.7	4.3	4.8–5.6
SD[e]	33 × 8	1.0	2.0	0.4	0.3–0.5

[a] FWHM major and minor axis deconvolved from the observed size, with the assumption of a 30″ beam.

[b] Average volume density derived from column density and size, with the assumption of a distance of 600 pc, except for CB 3 (2.5 kpc), CB 205 (2.5 kpc), and CB 244 (200 pc).

[c] Volume density range derived from excitation analysis of H_2CO.

[d] The cores associated with *IRAS* point sources were separated from the rest of the clouds to determine the sizes and other parameters.

[e] Averages and standard deviations excluding CB 3 and CB 205; for densities we give the mean and standard deviation of the logarithm of the density.

H_2CO is needed to improve our knowledge of n. The logarithmic average of $\langle n \rangle$ is 2×10^4 cm^{-3}, with a 1 σ dispersion of a factor of 2, for the sources in Table 4.

4.4. *Source Properties*

In this section, we compare the properties of globules with *IRAS* sources to those in the control sample. Because distances to the globules in this sample are mostly unknown, we will focus on quantities which are relatively insensitive to distance: peak antenna temperature (T_A^*), FWHM velocity width (Δv), aspect ratio for the mapped sources (long dimension over short dimension), and H_2 column density (N_{H_2}). Note that these quantities are only insensitive to distance if the source is well resolved, as is the case in this study. However, very distant sources that are well resolved will be selectively larger, and the line width–size relation may then introduce a weak distance dependence into the line width, since the line width of more distant sources will be averaged over a larger region.

The mean and standard deviation of the mean for T_A^* are 0.88 ± 0.11 K for the 23 cores with *IRAS* sources, indistinguishable from the mean of 1.0 ± 0.33 K for the four globules in the control sample. The mean line width is slightly larger for the cores with *IRAS* sources: 0.88 ± 0.10 km s^{-1} versus 0.65 ± 0.12 km s^{-1} for the control sample. The mean aspect ratio is 1.7 ± 0.2 for the 10 mapped cores with *IRAS* sources, marginally smaller than the mean value of 2.5 ± 1.5 for the two mapped cores without *IRAS* sources. The mean column density of H_2 is $(6.9 \pm 1.2) \times 10^{21}$ cm^{-2} for the 23 globules with *IRAS* sources, indistinguishable from the mean of $(6.2 \pm 2.0) \times 10^{21}$ cm^{-2} for the four globules without sources. In this sample, the presence of an *IRAS* source is not heralded by any other obvious change in properties.

The presence of an outflow seems more significant. Of those globules that YC searched for outflows, there are 13 $C^{18}O$ detections in sources with outflows and 13 $C^{18}O$ detections in sources without outflows. The mean T_A^* in sources with outflows is 1.0 ± 0.17 K, versus 0.73 ± 0.13 K for those without outflows; in addition, eight sources without outflows were not detected in $C^{18}O$, while only one source with an outflow was not detected. The mean line width is 1.05 ± 0.16 km s^{-1} in sources with outflows, somewhat larger than the mean of 0.72 ± 0.08 in sources without outflows. The resulting mean $N_{H_2} = (10.2 \pm 2.1) \times 10^{21}$ cm^{-2} in sources with outflows, versus $(5.0 \pm 0.65) \times 10^{21}$ cm^{-2} in sources without outflows. The mean aspect ratio of the eight mapped sources with outflows is 1.68 ± 0.20, indistinguishable from the mean of 1.59 ± 0.54 for the sources without outflows.

It would be interesting to compare these properties to those of cores in larger complexes, such as Taurus, but it only makes sense to compare properties determined from the same transition, since properties vary considerably with the molecule and transition. The only survey of Taurus cores in the $C^{18}O$ $J = 2 \rightarrow 1$ line that we could find was that of Zhou et al. (1994b), but one of the selection criteria used by that survey was that the sources be relatively isolated. Consequently, we found comparison to that sample to be of dubious significance.

5. COLLAPSE CANDIDATES

In this section, we identify collapse candidates based on (1) the location of the *IRAS* source relative to the $C^{18}O$ emission peaks and the nature of the *IRAS* emission, (2) a comparison of the widths of $C^{18}O$ and H_2CO lines, and (3) the shapes of the H_2CO lines. For the identified candidates, we also compare column density distributions with the distributions predicted from theoretical models of collapse.

5.1. *Coincidence with an IRAS Source*

For a core containing a collapsing protostar, the *IRAS* emission should come from the local peak of column density. Hence, the first condition for a collapse candidate is the coincidence of the *IRAS* source position with a $C^{18}O$ emission peak. In addition, *IRAS* sources with spectral energy distributions rising with wavelength into the far-infrared are more likely to be collapsing protostars than those with flat spectral energy distributions (Shu et al. 1987).

Of the 12 *IRAS* sources located within 34″ of the $C^{18}O$ emission peaks (§ 3.2), eight have stronger emission at 25 μm than at 12 μm (YC), suggestive of a heavily embedded object. In contrast, all six *IRAS* sources separated by more than 34″ have less emission at 25 μm than at 12 μm; these are unlikely to represent the current episode of star formation.

5.2. *Quiescent Cores versus Active Cores*

As discussed in § 1, a collapsing core should have an H_2CO line that is wider than its $C^{18}O$ line. Because increased turbulence in the denser regions could also produce the wider line, we use this criterion only to separate active cores, which include collapsing cores, from quiescent cores. We define an active core as one with $\Delta v(H_2CO)/\Delta v(C^{18}O) > 1 + \sigma_r$, where σ_r is the uncertainty in the line width ratio.

In our sample, the ratios of H_2CO and $C^{18}O$ line widths (see Table 3) vary from 0.5 (CB 68) to 5.2 (CB 3). Figure 3 plots the $H_2CO/C^{18}O$ intensity ratio versus the line width ratio for 11 dense cores with H_2CO detections. Three cores (CB 3, CB 54, and CB 244) are clearly active; they all have *IRAS* sources

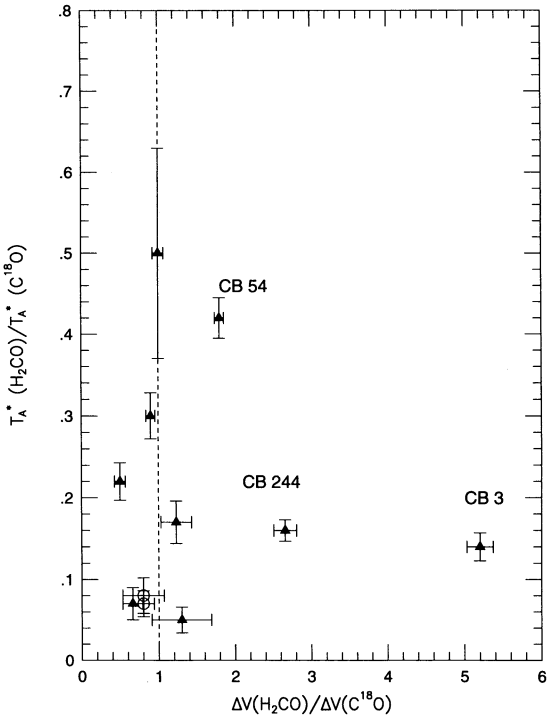

FIG. 3.—Ratios of line intensities and line widths of the H_2CO and $C^{18}O$ lines. Line parameters were derived from Gaussian fits to the profiles. Error bars were determined from the uncertainties in the Gaussian fits. The two circles represent CB 12 and CB 82, two globules without *IRAS* sources.

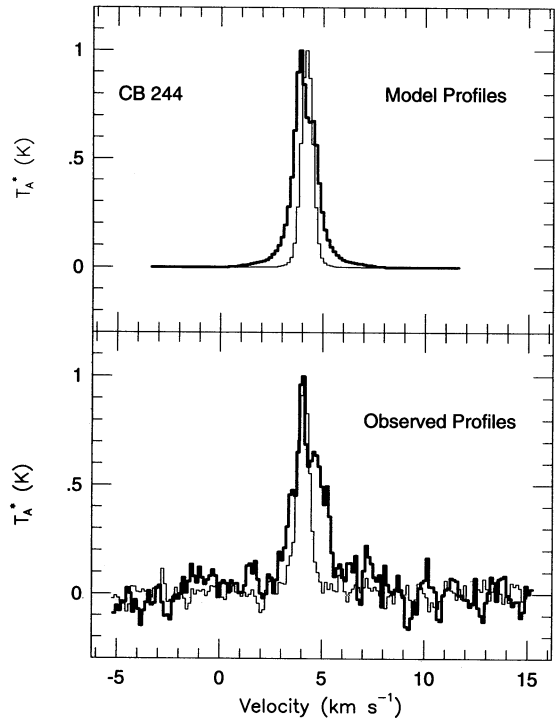

FIG. 4*a*

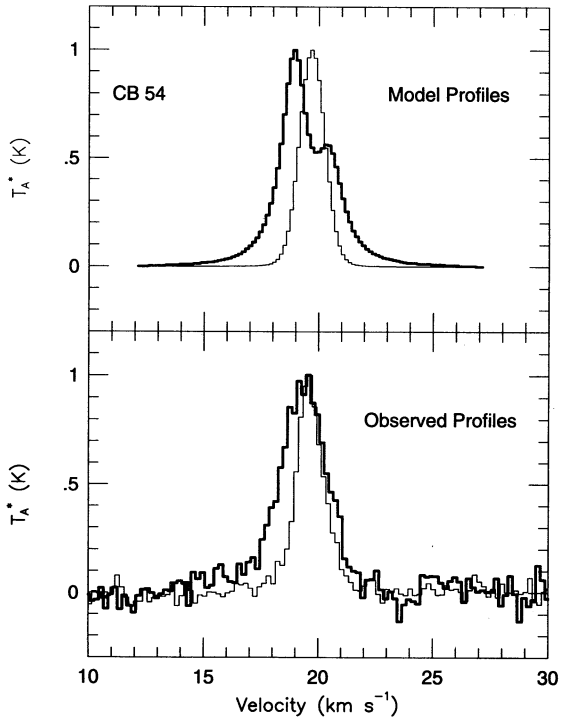

FIG. 4*b*

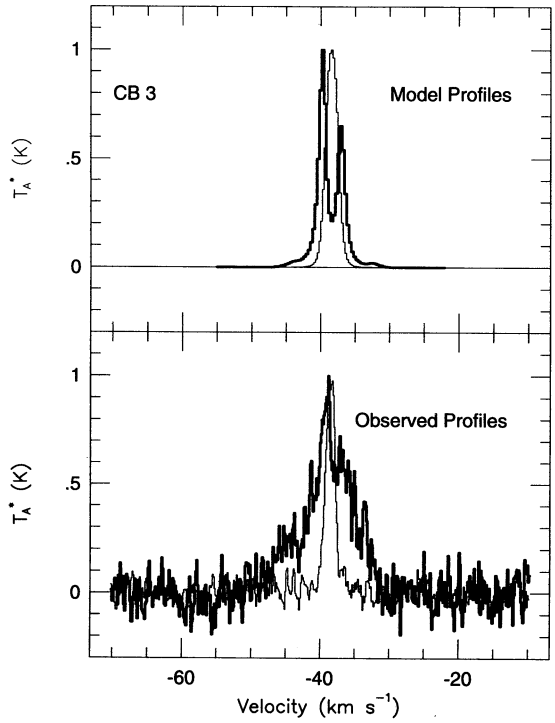

FIG. 4*c*

FIG. 4.—Model and observed profiles of H_2CO and the $C^{18}O$ lines, normalized to unity at the peak, in (*a*) CB 244, (*b*) CB 54, and (*c*) CB 3. The H_2CO line is plotted with a heavy line, and the $C^{18}O$ line is plotted with a light line. The top panel of each figure shows the model line profiles (calculated with the parameters in Table 5), while the bottom panel shows the observations on the same velocity scale. The profiles for CB 54 were taken in 1995 March, when the velocity scale was more certain.

within 34″ of the $C^{18}O$ emission peak. The increased line width ratio is not caused by narrower $C^{18}O$ lines. The intrinsic $C^{18}O$ line width of the overall globule sample has an average value of 0.8 ± 0.5 km s^{-1}, typical of low-mass dark clouds (Fuller & Myers 1993), while the line width for the three globules classified as dynamically active cores is 1.3 ± 0.5 km s^{-1}.

In the three active cores, H_2CO was also observed toward positions away from the $C^{18}O$ emission peak and *IRAS* source. At the offset positions, the H_2CO line width is similar to or less than the $C^{18}O$ line width, indicating no "activity" (see Figs. 2*a*–2*c*). Thus, the activity appears to be limited to a central region, a characteristic consistent with predictions of the inside-out collapse model.

5.3. *Line Profiles*

The last collapse criterion is that the line profiles must be consistent with those predicted for collapse. In particular, the H_2CO line in collapsing cores should appear asymmetric, with stronger blueshifted emission. The line profiles for the three active cores have the qualitative behavior expected for collapse (Fig. 4). For CB 3 and CB 244, the H_2CO spectra are double-peaked, with a stronger blue peak. For CB 54, the H_2CO spectrum is not double-peaked, but it is shifted to the blue (Fig. 4*b*); these CB 54 spectra were taken in 1995 March, when the more accurate frequencies were being calculated (see § 2.2).

A quantatitive comparison to the theory requires detailed modeling of the line profiles from a collapsing cloud. A Monte Carlo radiative transfer code and a beam convolution code (Choi et al. 1995) were used to produce model line profiles. The density and velocity fields were specified by the inside-out collapse model (Shu 1977). The temperature distribution was calculated by assuming that the gas kinetic temperature (T_K) is equal to the dust temperature (T_D) and that $T_D(r) = T_D(r_0)\,(r/r_0)^{-0.4}$, where r_0 is the outer radius of the model and

$T_D(r_0)$ was set by scaling the output of dust radiative transport models by $L^{0.2}$ (see, e.g., Doty & Leung 1994). The temperature law is a good approximation to the temperature in most of the region where the lines form, but once $T_D(r)$ drops below 10 K, $T_K(r)$ was set equal to 10 K to account for cosmic-ray heating in the low-density envelope (see Zhou et al. 1990 and Carr et al. 1995 for further discussion). The source luminosities were found by integrating the *IRAS* data and assuming a distance. For CB 54, the distance was assumed to be 600 pc; for the other two sources, we used the estimated distances in Table 5 (see § 4.2). The effective sound speeds ($a_{\rm eff}$) for the three cores were determined from the $C^{18}O$ line widths away from the *IRAS* sources, and the outer radii (r_0) were set equal to the mean radii of the 3 σ contours in the $C^{18}O$ maps.

The model parameters that remain are $r_{\rm inf}$, the infall radius (equivalently, the age since collapse began, since $r_{\rm inf} = t_{\rm inf}\, a_{\rm eff}$), the $1/e$ turbulent width ($\delta v_{\rm turb}$), and the abundance of the molecules being modeled. These were optimized by running a series of models and finding the best match to the observed line profiles. Matching the shape of the profile was considered more important than matching the strength, since simulations show that the latter depends more strongly on the (uncertain) distance. The peak antenna temperatures from the models are given in Table 5, as are the best-fitting values for $r_{\rm inf}$, $\delta v_{\rm turb}$, $X(C^{18}O)$, $X(H_2CO)$, and $t_{\rm inf}$. The infall radius and time depend directly on the distance, $\delta v_{\rm turb}$ is fairly insensitive to distance, and the abundances depend on the distances in a more complex way. The specific model parameters in Table 5 are not very precisely determined. They are intended as starting points for future modeling when more data are available.

Figure 4 shows the normalized H_2CO and $C^{18}O$ line profiles from the models. The model profiles match the observations reasonably well for CB 244. For CB 54, the model profile has a self-absorption dip that is not apparent in the data. Models with lower abundances of H_2CO predict less self-absorption, but they also predict weaker lines, worsening the discrepancy between the intensity predicted by the model and that actually observed (cf. Tables 3 and 5). This problem could be relieved if the density were higher than that in the Shu (1977) model. CB 3 is also problematic. The infall radius and abundance of H_2CO required for CB 3 is much higher than in the other sources. In addition, the intensity of the $C^{18}O$ line cannot be matched, even at the relatively high $C^{18}O$ abundance in Table 5. Both these facts suggest that CB 3 has higher densities than those predicted by the Shu model, a feature often seen in regions forming more massive stars (see, e.g., Zhou et al. 1991).

The model profiles for CB 3 can produce the relative strength of the two peaks in the H_2CO spectrum and the observed shift of the H_2CO peak relative to the $C^{18}O$ peak, but not the very broad wings on the H_2CO line. These may be caused by a very different infall velocity field or dense gas in the outflow. Wing emission in H_2CO is rare, but it has been seen (see Mangum et al. 1990). The CO wings cover a similar range of velocities (Yun & Clemens 1994a). Emission from gas outflowing in the plane of the sky could also fill in the self-absorption feature, which is less deep than in the models. A map of the H_2CO line, compared with a similar map of CO, could test this hypothesis.

We consider the three candidates to have passed this test, but only CB 244 looks like a good candidate for low-mass star formation as described by Shu (1977). CB 54 has the least convincing line profile, but it is worthy of further investigation. We emphasize that these tests are not definitive. To rule out explanations other than collapse, such as foreground absorption, contamination by outflowing gas, rotation, etc., maps in the H_2CO line and other tracers of the putative collapse region are needed. We consider these three globules to be collapse candidates and proceed to apply one more consistency check.

5.4. *Column Density Distributions*

For collapse candidates, the column density distribution measured in $C^{18}O$ may be compared with predictions of theoretical models. The H_2 column density is proportional to the integrated $C^{18}O$ line intensity if the $C^{18}O$ line is optically thin. Hence, the column density distribution is roughly described by the distribution of the azimuthally averaged, integrated intensity of the $C^{18}O$ line. Figure 5 shows these distributions for the three collapse candidates.

The same models which produced the line profiles in Figure 4 were used to construct model line profiles at positions displaced from the peak. These line profiles (simple Gaussian profiles decreasing in strength away from the center) were then fitted in the same way as were the observations, and the resulting distributions of integrated intensity are plotted as dotted lines in Figure 5. The model distribution agrees well with the observations of CB 244 out to a radius of about 40″, where the more extended cloud component becomes important. The model distributions in both CB 54 and CB 3 decline more rapidly than the observations, suggesting a flatter density distribution than predicted by the inside-out collapse model. The data do not warrant an exhaustive exploration of parameter space outside the context of established theoretical models, but we did try models in which the density is assumed to follow $n(r) \propto r^{-1}$ outside $r_{\rm inf}$ while, inside $r_{\rm inf}$, the density and velocity fields are unchanged from those that fit the line profiles. This rather ad hoc model did produce a flatter distribution of integrated intensity (dashed lines in Fig. 5), but the model emission still fell short of the observations at large angles. These modified density laws also affected the line profiles somewhat.

5.5. *Characteristics of Collapse Candidates*

The three tests applied in this section have identified three candidates for collapse. The test that eliminated the most candidates was the line width comparison. This test is effective in selecting strong candidates for further study. However, it may reject candidates that are at very early stages of collapse, when

TABLE 5

MODEL PARAMETERS FOR COLLAPSE CANDIDATES

Source	$L_{\rm FIR}$ ($L_\odot$)	d (pc)	$\delta v_{\rm turb}$ (km s^{-1})	$r_{\rm inf}$ (pc)	r_0 (pc)	T_A^* ($C^{18}O$) (K)	T_A^* (H_2CO) (K)	X ($C^{18}O$) (10^{-8})	X (H_2CO) (10^{-9})	$t_{\rm inf}$ (10^5 yr)
CB 3	830	2500	0.85	0.35	0.8	1.1	0.5	50	80	5.4
CB 54	55	600	0.65	0.08	0.12	1.2	0.3	7	8	1.6
CB 244.....	1	200	0.30	0.03	0.06	1.7	0.3	6	3	1.0

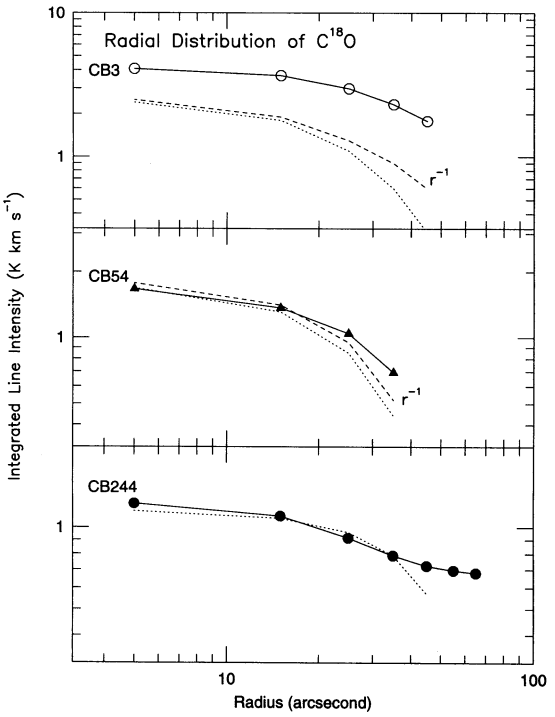

FIG. 5.—The azimuthally averaged $C^{18}O$ integrated intensity distributions in the three collapse candidates. The points connected by solid lines are the azimuthally averaged observations. The dotted lines are the predictions from the model that gave the best fit to the line profiles. Model parameters are given in Table 5. For CB 54 and CB 3, the dashed line represents the results of a model in which the density law is modified from r^{-2} to r^{-1} outside the collapse region. Inside r_{inf}, the density and velocity fields are unchanged.

the line width differences are less extreme (see § 1.2). Also, the H_2CO lines may become too weak to detect late in the collapse (see Zhou 1992). Thus, other globules with *IRAS* sources near $C^{18}O$ peaks are not *ruled out* as collapsing clouds. With this caveat in mind, we consider the three candidates in more detail.

CB 244 is the most classic example of low-mass star formation in this sample. The star-forming core has low mass (~ 1 $M_\odot$) and low luminosity (1 $L_\odot$). It has a high mean density (7×10^4 cm^{-3}) and a small core size. The small r_{inf} translates into a short time since collapse began (1×10^5 yr). The outflow is clearly bipolar, with a dynamical age of 9×10^3 yr, the result of Yun & Clemens (1994a) scaled to a distance of 200 pc. The position of the *IRAS* source agrees, within the *IRAS* PSC positional uncertainty of 18″, with the peaks of both $C^{18}O$ (Fig. 1*f*) and the center of the outflow (Yun & Clemens 1994a). These properties are reminiscent of those in B335, but the spectral energy distribution (SED) is quite different. While the infrared source in B335 is undetected at $\lambda < 60$ μm, CB 244 has a near-infrared source about 10″ from the *IRAS* position (Yun 1993). High-resolution images at mid-infrared wavelengths will be needed to determine if the near-infrared source is actually related to the *IRAS* source and the column density peak.

CB 54 appears to be slightly more massive (~ 7 $M_\odot$) and is clearly more luminous (55 $L_\odot$) than CB 244, but both quantities depend rather strongly on the unknown distance. The mean density is also relatively high (4×10^4 cm^{-3}). The column density has a single peak, centered on the *IRAS* source, but falls off more slowly with radius than expected from the collapse model. The infall age would be about 1.6×10^5 yr, safely in excess of the dynamical age of 2.8×10^4 yr for the clearly bipolar outflow (Yun & Clemens 1994a). The signature of collapse is not particularly dramatic in this source. The *IRAS* PSC position (uncertainty of 21″) agrees very well with the $C^{18}O$ peak (Fig. 1*b*) and the apparent outflow source (Yun & Clemens 1994a). The SED increases from 2 to 100 μm; there are actually two near-infrared sources, within common nebulosity, near the *IRAS* position (Yun & Clemens 1994b; Yun 1993), raising the possibility of multiple star formation. High-resolution images at mid-infrared wavelengths will be crucial in determining which, if either, of these sources is associated with the peak of luminosity and column density.

CB 3 is an anomaly in this sample. At a distance of 2.5 kpc, its core is much more massive (~ 70 $M_\odot$) and luminous (830 $L_\odot$) than the other globules in this sample. It is probably a case of intermediate-mass, rather than low-mass, star formation. Its infall age is 5.4×10^5 yr, longer than the outflow dynamical time, scaled to 2.5 kpc, of 6×10^4 yr (Yun & Clemens 1994a). Its line profiles and $C^{18}O$ distribution are least well matched by the models, as discussed above, though the signature of collapse is reasonably clear. The outflow is less bipolar, which perhaps explains why the H_2CO spectrum is more contaminated by outflowing gas. The SED rises quite steeply from 25 to 100 μm, but a number of near-infrared sources, one of which is nebulous (Yun & Clemens 1994b), produce a second peak in the SED at shorter wavelengths. The near-infrared sources are 13″ from the *IRAS* position (Yun 1993). The *IRAS* source itself is about 30″ from the peak of the $C^{18}O$ emission (Fig. 1*a*) and the apparent source of the outflow (Yun & Clemens 1994a), but the positional uncertainty in the *IRAS* PSC is 15″. Again, high-resolution mid-infrared images are necessary to determine which, if any, of these sources are at the center of luminosity and column density.

6. SUMMARY AND FUTURE WORK

We detected $C^{18}O$ emission in the $J = 2 \rightarrow 1$ line toward 70% of a sample of about 40 globules selected as likely to be forming stars. Maps of $C^{18}O$ located column density maxima within 30″ of *IRAS* source in 12 globules. The $J_{K_{-1}K_1} = 3_{12} \rightarrow 2_{11}$ line of H_2CO was detected toward nine of these 12 positions, indicating a high volume density, as well as high column density. Three of these nine H_2CO lines are significantly wider than the $C^{18}O$ lines, which suggests enhanced activity in the cloud core. The shapes of the line profiles are qualitatively consistent with collapse in all three, CB 54 being the least consistent. Models of line profiles expected in an inside-out collapse are also consistent with the observations, but uncertainties in distance and the velocity scale prevent a definitive conclusion. We conducted a consistency check by using the model that best matched the line profiles to predict the spatial distribution of the $C^{18}O$ emission. The prediction agreed with the observations in CB 244 out to radii where the extended cloud component confused the issue; the predictions fell off faster than the observations in CB 54 and CB 3.

We conclude that CB 244 is a good candidate to be a collapsing core that is forming a low-mass star. CB 54 is also a possible candidate, but it may be forming multiple stars. CB 3 is a much more massive cloud, with a luminosity characteristic of intermediate-mass star formation. If the outflow can be separated from infall motions, it may provide a good example of collapse in a more massive environment.

To further our understanding of these objects, several additional studies are needed. Most urgently, distances must be determined toward these globules. High-resolution studies in the mid-infrared are needed to determine positions of the

centers of luminosity and column density and to decide which near-infrared sources, if any, are associated with the far-infrared emission. Observations of other lines of H_2CO and other density-sensitive molecules like CS are needed to constrain the density distribution. Maps and line profiles obtained with higher spatial resolution are needed to separate possible contributions from outflowing gas and to probe the kinematics to smaller scales, where collapse (and possibly rotation) become more important.

This work was supported by NSF grant AST 93-17567 and by a grant from the Keck Foundation to the University of Texas and by NSF grant AST 92-21194 to Boston University. We thank M. Choi for access to his Monte Carlo code and assistance in using it and J. Scalo for helpful discussion. E. Gregersen assisted with some calculations. K. Tatematsu, Connie Walker, and U. Graf assisted with observations, as did the CSO staff, including the late Larry Strom. We dedicate this paper to his memory.

REFERENCES

Adelson, L. M., & Leung, C. M. 1988, MNRAS, 235, 349
Barnard, E. E. 1927, in A Photographic Atlas of Selected Regions of the Milky Way, ed. E. B. Frost & M. R. Calvert (Washington: Carnegie Inst. Washington Publ.), 1
Beichman, C. A., Neugebauer, G., Habing, H. J., Clegg, P. E., & Chester, T. J. 1987, Explanatory Supplement to the *IRAS* Catalogs and Atlases (Washington: US GPO)
Bok, B. J. 1948, Centennial Symposia, Harv. Obs. Monogr., 7, 53
Bok, B. J., & McCarthy, C. C. 1974, AJ, 79, 42
Bok, B. J., & Reilly, E. F. 1947, ApJ, 105, 255
Carr, J. S., Evans, N. J., II, Lacy, J. H., & Zhou, S. 1995, ApJ, 450, 667
Cernicharo, J., & Guélin, M. 1987, A&A, 176, 299
Chandler, C. J., & Sargent, A. I. 1993, ApJ, 414, L29
Choi, M., Evans, N. J., II, Gregersen, E., & Wang, Y. 1995, ApJ, 448, 742
Choi, M., Evans, N. J., II, & Jaffe, D. T. 1993, ApJ, 417, 624
Clemens, D. P., & Barvainis, R. 1988, ApJS, 68, 257
Clemens, D. P., Yun, J. L., & Heyer, M. H. 1991, ApJS, 75, 877
de Jong, T., Chu, S. I., & Dalgarno, A. 1975, ApJ, 199, 69
Dickman, R. L. 1976, Ph.D. thesis, Columbia Univ.
Doty, S. D., & Leung, C. M. 1994, ApJ, 424, 729
Falgarone, E., Lis, D. C., Phillips, T. G., Pouquet, A., Porter, D. H., & Woodward, P. R. 1994, ApJ, 436, 728
Frerking, M. A., Langer, W. D., & Wilson, R. W. 1982, ApJ, 262, 590
Fuller, G. A., & Myers, P. C. 1992, ApJ, 384, 523
———. 1993, ApJ, 418, 273
Keene, J., Davidson, J. A., Harper, D. A., Hildebrand, R. H., Jaffe, D. T., Lowenstein, R. F., Low, F. J., & Pernic, R. 1983, ApJ, 274, L43
Keto, E. R., & Lattanzio, J. C. 1989, ApJ, 355, 190
Kutner, M. L., & Ulich, B. L. 1981, ApJ, 250, 341
Leung, C. M., Kutner, M. L., & Mead, K. N. 1982, ApJ, 262, 583
Lizano, S., & Shu, F. H. 1989, ApJ, 342, 834
Lovas, F. J. 1986, J. Phys. Chem. Ref. Data, 15, 251
Lynds, B. T. 1962, ApJS, 7, 1
———. 1965, ApJS, 12, 163
Mangum, J. G. 1993, PASP, 105, 117
Mangum, J. G., Wootten, A., Loren, R. B., & Wadiak, E. J. 1990, ApJ, 348, 542
Martin, R. N., & Barrett, A. H. 1978, ApJS, 36, 1
Myers, P. C., Linke, R., & Benson, P. J. 1983, ApJ, 264, 517
Nozawa, S., Mizuno, A., Teshima, Y., Ogawa, H., & Fukui, Y. 1991, ApJS, 77, 647
Penzias, A., & Burrus, C. 1973, ARA&A, 11, 51
Rickard, L. J., Palmer, P., Buhl, D., & Zuckerman, B. 1977, ApJ, 213, 654
Scappini, F., Caselli, P., & Palumbo, G. G. C. 1991, MNRAS, 249, 763
Schmidt, E. G. 1975, MNRAS, 172, 401
Shu, F. H. 1977, ApJ, 214, 488
Shu, F. H., Adams, F. C., & Lizano, S. 1987, ARA&A, 25, 23
Tomita, Y., Saito, T., & Ohtani, H. 1979, PASJ, 31, 407
Turner, B. E. 1994a, ApJ, 420, 661
———. 1994b, ApJ, 437, 658
Turner, D. G. 1986, A&A, 167, 157
van Dishoeck, E. F., & Black, J. H. 1988, ApJ, 334, 771
Villere, K. R., & Black, D. C. 1980, ApJ, 236, 192
Winnewisser, M., Winnewisser, B. P., & Winnewisser, G. 1985, in Molecular Astrophysics, ed. G. Diercksen, W. Huebner, & P. Langhoff (Dordrecht: Reidel), 375
Xie, T., & Goldsmith, P. F. 1990, ApJ, 359, 378
Yun, J. L. 1993, Ph.D. thesis, Boston Univ.
Yun, J. L., & Clemens, D. P. 1990, ApJ, 365, L73
———. 1992, ApJ, 385, L21
———. 1994a, ApJS, 92, 145
———. 1994b, AJ, 108, 612
Zhou, S. 1992, ApJ, 394, 204
Zhou, S., Evans, N. J., II, Butner, H., Kutner, M. L., & Mundy, L. G. 1990, ApJ, 363, 168
Zhou, S., Evans, N. J., II, Güsten, R., Mundy, L. G., & Kutner, M. L. 1991, ApJ, 372, 518
Zhou, S., Evans, N. J., II, Kömpe, C., & Walmsley, C. M. 1993, ApJ, 404, 232
———. 1994a, ApJ, 421, 854
Zhou, S., Evans, N. J., II, Wang, Y., Peng, R., & Lo, K. Y. 1994b, ApJ, 433, 131